Lysosome acidification by photoactivated nanoparticles restores autophagy under lipotoxicity

Kyle M. Trudeau,[1] Aaron H. Colby,[2,3] Jialiu Zeng,[2] Guy Las,[4] Jiazuo H. Feng,[2] Mark W. Grinstaff,[2] and Orian S. Shirihai[1,4,5]

[1]Obesity and Nutrition Section, Department of Medicine, Evans Biomedical Research Center, Boston University School of Medicine, Boston, MA 02118
[2]Departments of Biomedical Engineering, Chemistry, and Medicine, Boston University, Boston, MA 02215
[3]Department of Surgery, Brigham and Women's Hospital, Harvard Medical School, Boston, MA 02215
[4]Department of Clinical Biochemistry and Pharmacology, Faculty of Health Sciences, Ben-Gurion University of the Negev, Beer-Sheva 84103, Israel
[5]Division of Endocrinology, Department of Medicine, David Geffen School of Medicine, University of California, Los Angeles, Los Angeles, CA 90045

In pancreatic β-cells, liver hepatocytes, and cardiomyocytes, chronic exposure to high levels of fatty acids (lipotoxicity) inhibits autophagic flux and concomitantly decreases lysosomal acidity. Whether impaired lysosomal acidification is causally inhibiting autophagic flux and cellular functions could not, up to the present, be determined because of the lack of an approach to modify lysosomal acidity. To address this question, lysosome-localizing nanoparticles are described that, upon UV photoactivation, enable controlled acidification of impaired lysosomes. The photoactivatable, acidifying nanoparticles (paNPs) demonstrate lysosomal uptake in INS1 and mouse β-cells. Photoactivation of paNPs in fatty acid–treated INS1 cells enhances lysosomal acidity and function while decreasing p62 and LC3-II levels, indicating rescue of autophagic flux upon acute lysosomal acidification. Furthermore, paNPs improve glucose-stimulated insulin secretion that is reduced under lipotoxicity in INS1 cells and mouse islets. These results establish a causative role for impaired lysosomal acidification in the deregulation of autophagy and β-cell function under lipotoxicity.

Introduction

Autophagy is an essential cellular maintenance mechanism, especially in nonproliferating cells, by which cells target and degrade long-lived proteins and organelles (Terman et al., 2010; Schneider and Cuervo, 2014; Kroemer, 2015). The two key steps of autophagy are autophagosome formation around the cellular contents to be degraded and, subsequently, autophagosome fusion with a lysosome. Both fusion of lysosomes with autophagosomes as well as activation of lysosomal hydrolases are dependent on maintenance of a sufficiently low pH of the lysosome (Yamamoto et al., 1998; Kawai et al., 2007).

In pancreatic β-cells (Ebato et al., 2008; Choi et al., 2009), liver hepatocytes (González-Rodríguez et al., 2014; Park and Lee, 2014), and cardiomyocytes (Park et al., 2015), exposure to high levels of fatty acids, termed lipotoxicity (LT), has been shown to increase autophagosome number per cell; this could be caused by increased formation or decreased degradation of autophagosomes (Klionsky et al., 2012). Recent studies suggest that central to LT pathophysiology is the inhibition of autophagic flux with concomitant reduction in lysosomal acidity and function in the different cell types (Inami et al., 2011; Fukuo et al., 2014; Jaishy et al., 2015), including pancreatic β-cells (Las et al., 2011; Mir et al., 2015). It is therefore hypothesized that lysosome-dependent clearance of autophagosomes is blocked in cells exposed to LT, leading to accumulation of autophagosomes (Jaishy et al., 2015). However, the role of impaired lysosomal acidification in the deregulation of autophagic flux and in the resulting cellular dysfunction could not be addressed, as no mechanism was available to specifically restore acidification in the lysosome.

Addressing this question would require a method for delivering acid to the lysosome in a robust, organelle-specific, dose-dependent, and time-controlled manner. We rationalized that these requirements could be addressed through the utilization of polymeric nanoparticles (NPs). NPs represent an efficient means for targeting the lysosome because of their uptake through endocytotic pathways (Bareford and Swaan, 2007; Baltazar et al., 2012; Zubris et al., 2013; Zhang, 2015). Subsequent trafficking of NPs into cellular endosomes and eventual accumulation in lysosomes (Bareford and Swaan, 2007; Zubris et al., 2013) provides an ideal route for treating lysosomal dysfunction, either through delivery of a drug or by the action of the NP or material itself. For example, Baltazar et al. (2012) demonstrated that when poly(DL-lactic-*co*-glycolide acid) NPs

Correspondence to Orian Shirihai: oshirihai@mednet.ucla.edu; or Mark W. Grinstaff: mgrin@bu.edu

Abbreviations used in this paper: DMAP, 4-dimethylaminopyridine; GSIS, glucose-stimulated insulin secretion; LC-MS, liquid chromatography mass spectrometry; LT, lipotoxicity; NMR, nuclear magnetic resonance; NP, nanoparticle; paNP, photoactivatable, acidic nanoparticle.

The Rockefeller University Press $30.00
J. Cell Biol. Vol. 214 No. 1 25–34
www.jcb.org/cgi/doi/10.1083/jcb.201511042

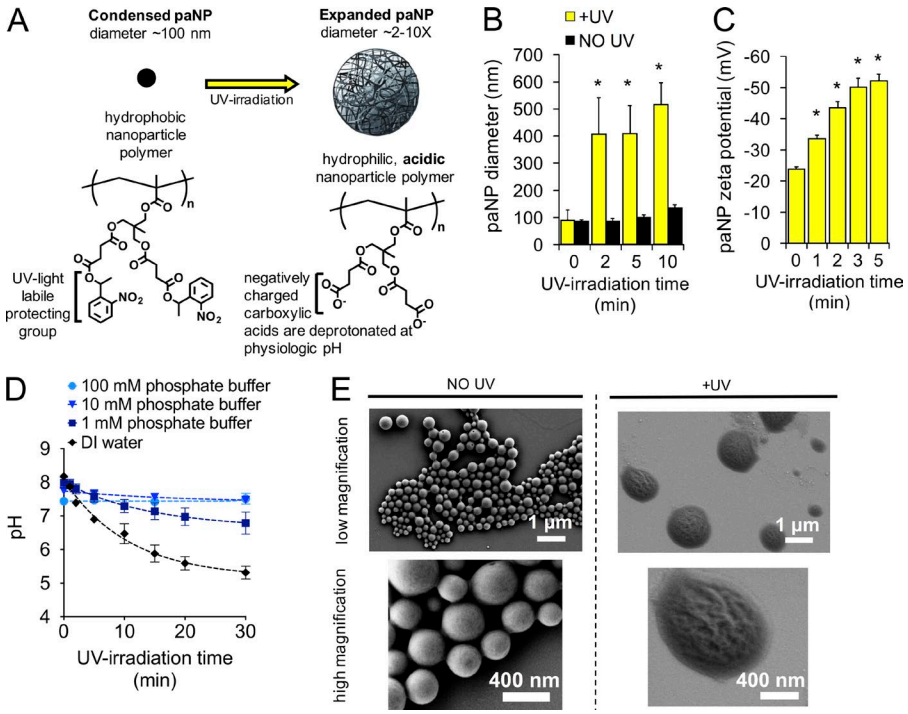

Figure 1. **Characterization of UV activation of paNPs.** (A) Schematic of the paNP mechanism of UV-triggered acidification and swelling. (B) Dynamic light scattering characterization measurements of paNP diameter as a function of UV irradiation and duration. paNPs exposed to UV light (yellow bars) increase in diameter by 300–400%; without UV exposure, paNP diameter remains constant (n = 3 experiments; *, $P < 0.05$ vs. time 0). (C) Zeta potential (i.e., surface charge) of the paNPs becomes more negative with additional UV irradiation because of the deprotection of additional carboxylic acid functionalities (n = 3 experiments; *, $P < 0.01$ vs. time 0). (D) pH of deionized water or pH 7.4 phosphate buffers of increasing buffering strengths (i.e., molarities) as a function of UV irradiation time. (E) Scanning electron micrograph images of paNPs before (left) and after (right) UV irradiation demonstrate UV-triggered swelling. All error data are plotted as mean ± SD.

(PLGA-NPs) are given (1 mg/ml) to ARPE-19 cells affected by lysosomal dysfunction, degradation of the PLGA-NPs into acidic byproducts facilitated reacidification of lysosomes.

Building from this concept, we have designed and evaluated a stimulus-responsive NP that allows for externally triggered activation and acidification of the lysosome. Although stimuli-responsive NPs have frequently been used in other contexts, such as drug delivery, this is the first study to use such a system to provide active control over lysosomal and autophagic recovery in which the NP itself is the active agent (Kost and Langer, 2001; Ganta et al., 2008; Motornov et al., 2009; Colson and Grinstaff, 2012; Moghimi et al., 2012; Wolinsky et al., 2012). Herein, we describe the synthesis and characterization of a photoactivatable NP that, in the presence of water and UV light (365 nm), expands and becomes acidic. These particles are thus termed photoactivatable, acidic NPs (paNPs; Fig. 1 A). We investigate the internalization and localization of paNPs in INS1 cells as well as the subsequent effect of paNP-mediated lysosomal acidification on recovery of autophagic flux and β-cell ability to secrete insulin, a functionality that is depressed under LT (Molina et al., 2009; Poitout et al., 2010; Las et al., 2011).

Results and discussion

Synthesis and characterization of paNPs

By engineering the polymer structure of paNPs to contain acid functionalities with UV-labile protecting groups, acidification is constrained to occur only in response to UV light. UV deprotection was confirmed by liquid chromatography-mass spectrometry (LC-MS; Fig. S2 A). Dynamic light scattering demonstrates a significant (three- to fourfold) increase in overall paNP diameter when exposed to UV light (365 nm) but no size change without UV exposure (Fig. 1 B). Scanning electron microscopy reveals a clear, gross increase in particle size with a change in surface topology and morphology; however, as a result of the vacuum drying required to prepare particle samples, the resultant images must be interpreted with caution (Fig. 1 E). The apparently "cracked" topology may be reflective of the drying pattern of the less dense, swollen paNP, which is consistent with previously published transmission electron microscopy data of expansile nanoparticles in the swollen state (Colby et al., 2013). Furthermore, these previous studies demonstrate that swollen NPs are soft and deformable in nature with little mechanical integrity, and it is therefore likely that swollen paNPs exert negligible force on lysosomal membranes after internalization and UV activation. The surface charge (i.e., zeta potential) of paNPs becomes increasingly negative with additional UV irradiation (Fig. 1 C), confirming the deprotection process and reflecting the exposure of greater numbers of carboxylic acid groups, which are negatively charged at neutral pH. Lastly, paNPs under UV exposure significantly acidified deionized water (Fig. 1 D), but their effect is markedly decreased by the buffering capacity of a phosphate buffer. Although paNPs do not decrease the pH of the buffered solutions below pH 6.5, this is merely a reflection of the polymer concentration used; a lower pH could be achieved by increasing the concentration of paNPs.

Cytotoxicity, uptake, and intracellular localization of paNPs

The cytotoxicity of paNPs was determined in the INS1 insulinoma line. In brief, cells were loaded with paNPs for 4 h and then photoactivated (or not) with UV light for 5 min, followed by an additional 20 h of incubation. After the 20-h incubation, viability was determined using propidium iodide staining and flow cytometry. No significant cytotoxicity was observed up to 25 µg/ml with or without UV photoactivation (Fig. 2 A). However, at a dose of 250 µg/ml, there was significant toxicity in cells treated with paNPs followed by photoactivation. This cytotoxic effect was entirely absent in cells treated with UV in the absence of paNPs and in cells treated with 250 µg/ml paNPs but without exposure to UV, which demonstrates the UV-dependent activation of the particles in intact cells. A dose of 25 µg/ml was selected for further studies to avoid cytotoxic effects upon UV irradiation.

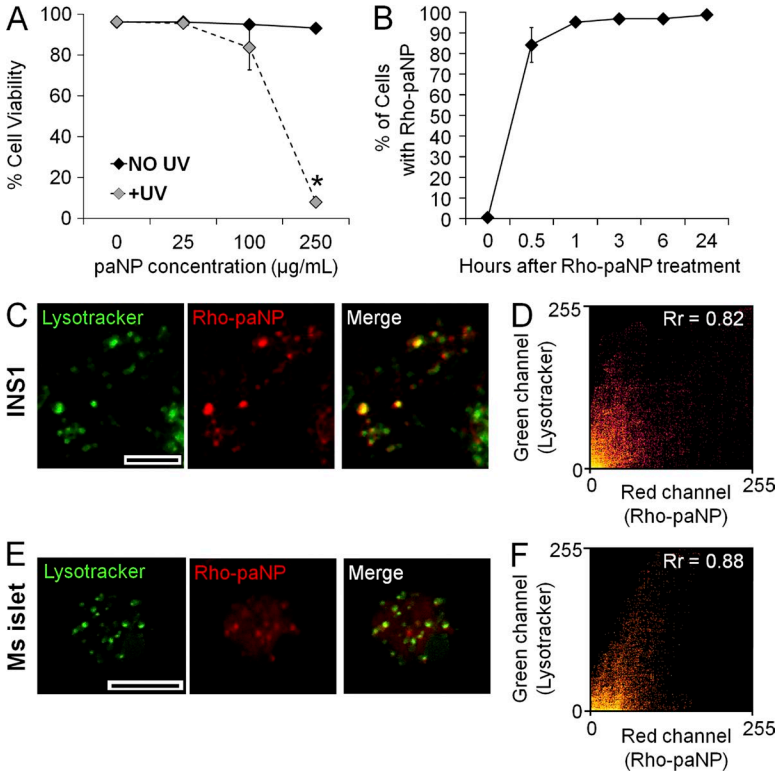

Figure 2. **paNP cytotoxicity and localization in INS1 and mouse islet cells.** (A) Dependency of paNP toxicity on dose and UV activation. Cells were incubated with a range of paNP concentrations for 4 h. paNPs were then UV activated by 5 min of cellular exposure to UV. paNPs at 250 µg/ml induced significant cell death only when UV irradiated, indicating robust UV activation of paNPs in intact cells. To avoid cytotoxicity of UV-irradiated paNPs, a treatment dose of 25 µg/ml was chosen for further studies. Shown is the mean ± standard error; *, $P < 0.01$ versus NO UV 250 µg/ml paNP ($n = 3$ experiments). (B) Quantification of rhodamine-labeled paNP (Rho-paNP) uptake in INS1 cells by flow cytometry. Rho-paNP uptake occurs within 1 h, with complete uptake after 24 h incubation. Shown is the mean ± SD ($n = 3$ experiments). (C) Confocal microscopy images of Rho-paNPs in INS1 cells. Rho-paNPs (red) localize within the lysosomal compartments (Lysotracker; green channel) of INS1 cells. Bar, 10 µm. (D) Frequency scatterplot of Lysotracker (green channel) and Rho-paNP (red channel) from C. Rr value is Pearson's coefficient, which is consistent with high colocalization of Rho-paNPs and lysosomes. (E) Images of Rho-paNPs in mouse (Ms) islet cells. Rho-paNPs (red) localize within the lysosomal compartments (Lysotracker; green channel) of primary mouse islet cells. Bar, 10 µm. (F) Frequency scatterplot from (E) image. A high degree of colocalization of Rho-paNPs and lysosomes is observed.

Using the selected 25 µg/ml dose, rhodamine-labeled paNPs were incubated with INS1 cells for different durations (see Fig. S1 for synthesis details of the covalently conjugated rhodamine-labeled paNPs). Flow cytometry demonstrated rapid cellular uptake of paNPs (Fig. 2 B). Over 80% of cells showed paNP uptake within 30 min and nearly 100% of cells as early as 3 h. Furthermore, cells showed a dose-dependent uptake of paNPs (Fig. S2 B). Finally, we sought to determine the subcellular location of paNPs within the cell, as the size of the paNPs (~100 nm) was expected to lead to uptake and localization within the endosome-lysosome system (Petros and DeSimone, 2010). Colocalization imaging with Lysotracker dye confirmed cellular trafficking of paNPs into lysosomes in INS1 (Fig. 2, C and D) and primary mouse islet (Fig. 2, E and F) cells.

Acute activation of paNPs restores lysosomal acidity in β-cells exposed to fatty acids

Having demonstrated paNP function and cellular uptake into lysosomes, the essential subsequent question for these studies was whether paNPs could restore lysosomal acidity in cells exposed to LT. INS1 cells were exposed to 0.4 mM palmitate complexed to BSA (Palm:BSA) at a 4:1 ratio or a control amount of BSA for 20 h and concurrently incubated with or without 25 µg/ml paNPs. After 20 h, cells were either UV irradiated for 5 min or left untreated; 1 h later, lysosomal acidity was assessed by Lysosensor staining and confocal imaging (Fig. 3 A). To demonstrate specificity of Lysosensor staining of lysosomes, cells were treated with 100 µM bafilomycin for 2 h before imaging, which shows no Lysosensor staining because of neutralization of lysosomal pH. Palmitate exposure significantly increased lysosomal pH and size compared with control BSA-treated cells (Fig. 3, B and C). Treatment with paNPs without photoactivation had no significant effect on changing lysosomal pH or mean size in palmitate-treated cells. In contrast, treatment with paNPs that were subsequently UV-activated induced a significant decrease in lysosomal pH in palmitate-treated cells (Fig. 3 C). Treatment with PLGA nanoparticles, which have been previously shown to acidify lysosomes when used at a concentration of 1 mg/ml (Baltazar et al., 2012; Lee et al., 2015), partially restored lysosomal acidity under palmitate at a concentration of 1 mg/ml. In comparison, UV-activated paNPs restored lysosomal acidity at a 40-fold lower concentration of 25 µg/ml (Fig. S2 C). A reduction in mean lysosomal size was also observed with paNPs that were UV activated; however, this was not statistically significant from the palmitate-treated cells (Fig. 3 C). Although the paNPs expand upon photoactivation, they do not expand into a rigid structure (Colby et al., 2013) and, therefore, are not expected to exert force on the lysosomal membrane or affect lysosomal size.

The activity of lysosomal cathepsins is pH dependent. Previous studies demonstrated that exposure to fatty acids results in the inhibition of cathepsin activity (Las et al., 2011). Restoration of lysosomal acidity with paNPs significantly increased the pH-dependent activity of lysosomal cathepsin L under palmitate, as measured by Magic red cathepsin L fluorescent substrate assay (Fig. 3 D). Thus, paNPs enable acute acidification and functional rescue of lysosomes under lipotoxicity within 1–2 h after UV irradiation.

Lysosomal acidification controlled by paNPs restores autophagic flux in β-cells exposed to fatty acids

To investigate whether restoration of lysosomal acidity relieved the inhibition of autophagic flux in INS1 cells exposed to palmitate, we monitored intracellular accumulation of microtubule-associated protein 1A/1B light chain 3 (LC3-II), a marker for autophagosomes (Klionsky et al., 2012). Western blot analysis

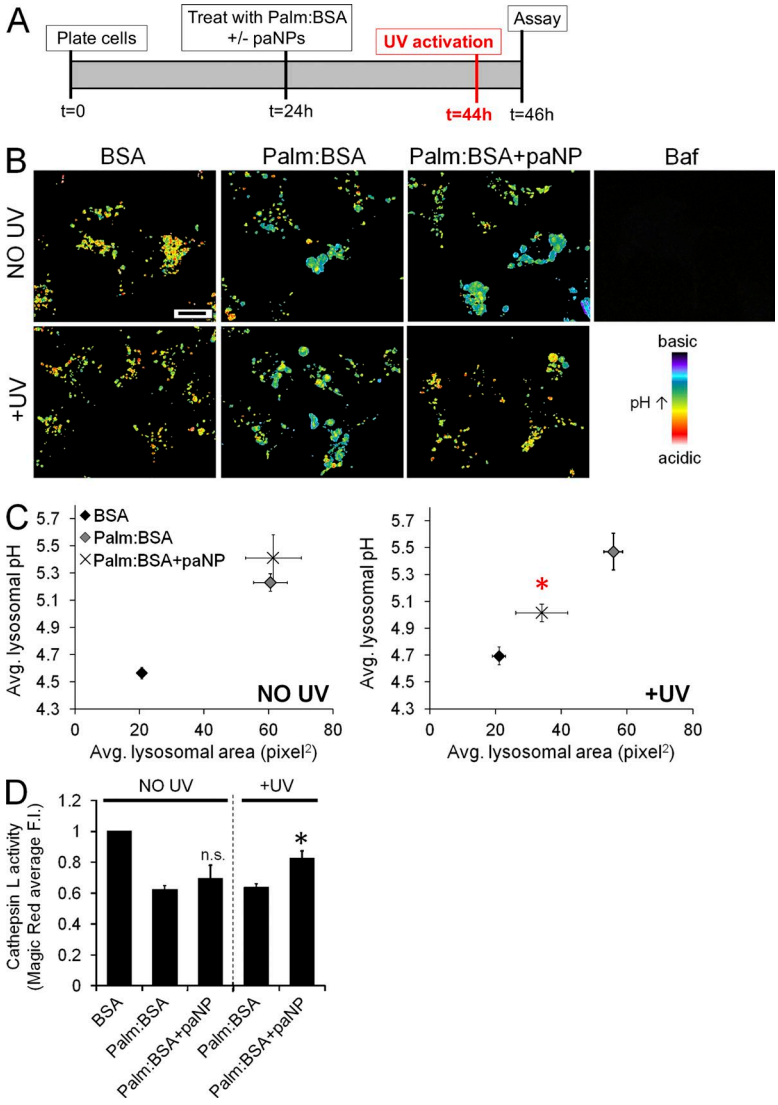

Figure 3. **Effect of paNPs on lysosomal pH in INS1 cells exposed to palmitate.** (A) Schematic of experimental protocol for Palm:BSA and paNP treatment followed by acute UV activation before assaying lysosomal acidity, autophagy, or cellular function. (B) Pseudo-colored confocal microscopy images of INS1 cells treated with the indicated conditions and stained with pH-sensitive Lysosensor dye to assess lysosome acidity. 100 µM bafilomycin (Baf) was used to demonstrate specificity of Lysosensor staining of lysosomes. Bar, 10 µm. (C) Mean lysosomal pH and lysosomal area per cell for cells exposed to control BSA, palmitate (Palm:BSA), or palmitate with paNP treatment (Palm:BSA+paNP), then UV irradiated (+UV) or not irradiated (NO UV). Cells treated with Palm:BSA+paNP and UV irradiated show significant restoration of lysosomal pH compared with Palm:BSA cells. Shown is the mean ± standard error; *, $P < 0.05$ versus Palm :BSA. $n = 3$ experiments for pH values and $n = 2$ experiments for size values with 20–30 cells analyzed per experiment. (D) Assessment of lysosomal cathepsin L activity by Magic red cathepsin L fluorescent substrate assay in INS1 cells exposed to control BSA, palmitate (Palm:BSA), or palmitate with paNP treatment (Palm:BSA+paNP), then UV irradiated (+UV) or not irradiated (NO UV). Restoration of lysosomal acidity with paNPs significantly increased the pH-dependent activity of lysosomal cathepsin L under palmitate. Shown is the mean ± standard error; *, $P < 0.05$ between indicated conditions ($n = 5$ experiments); n.s., not significant.

of LC3-II demonstrated a significant accumulation of autophagosomes in INS1 cells after palmitate treatment. Clearance of autophagosomes in palmitate-treated cells was observed after treatment with paNPs and subsequent UV activation (Fig. 4, A and B). Reduction in the number of autophagosomes was also seen by imaging GFP-LC3 puncta in INS1 cells, which showed a decrease in the number of autophagosomes after photoactivation of paNP-treated cells (Fig. 4 D). To further confirm the effect of paNPs on autophagic degradation, we monitored levels of p62 protein, a protein that is degraded during autophagy and used as a marker for autophagic flux (Klionsky et al., 2012). Palmitate exposure increased p62 levels, indicating inhibition of autophagic flux and accumulation of autophagic substrates. paNP treatment followed by UV activation significantly decreased (i.e., returned toward control values) p62 levels, suggesting an increase in autophagic flux when lysosomal acidity is restored by UV activation of paNPs (Fig. 4 C).

Promoting autophagic flux with paNPs enhances glucose-stimulated insulin secretion in β-cells exposed to fatty acids

Lastly, having observed the recovery of both lysosomal acidity and autophagic flux, we investigated whether paNP treatment could improve β-cell function (i.e., insulin secretion) in INS1 cells and primary mouse islets exposed to fatty acids. After 18 h of exposure to 0.4 mM palmitate, INS1 cells show inhibited glucose-stimulated insulin secretion (GSIS), an indicator of β-cell dysfunction. Treatment with paNPs followed by 5 min of UV irradiation acutely enhanced GSIS in INS1 cells under palmitate (Fig. 5 A). Treatment with paNPs alone (No UV activation) showed a trend toward increasing GSIS, but was not significant. Also paNP treatment followed by UV activation showed a nonsignificant trend toward increasing GSIS under control BSA condition (Fig. S3 A). To control for a potential effect of the UV exposure on insulin content and thereby on secretion, insulin content was measured. Insulin content was not significantly altered in any of the conditions (Fig. S3 B). Moreover, paNPs did not colocalize with insulin granules in INS1 cells (Fig. S3 C). Altogether, these findings suggest that paNPs are unlikely to directly affect insulin release from granules. Because the lysosomal pH is a result of the action of the lysosomal V-ATPase plus an additional pH reduction contributed by the paNPs, we rationalized that inhibition of the V-ATPase using bafilomycin would return lysosomal pH to the pH before paNPs activation. Indeed, the paNP-induced increase in GSIS was blocked when cells were preincubated with 10 nM bafilomycin

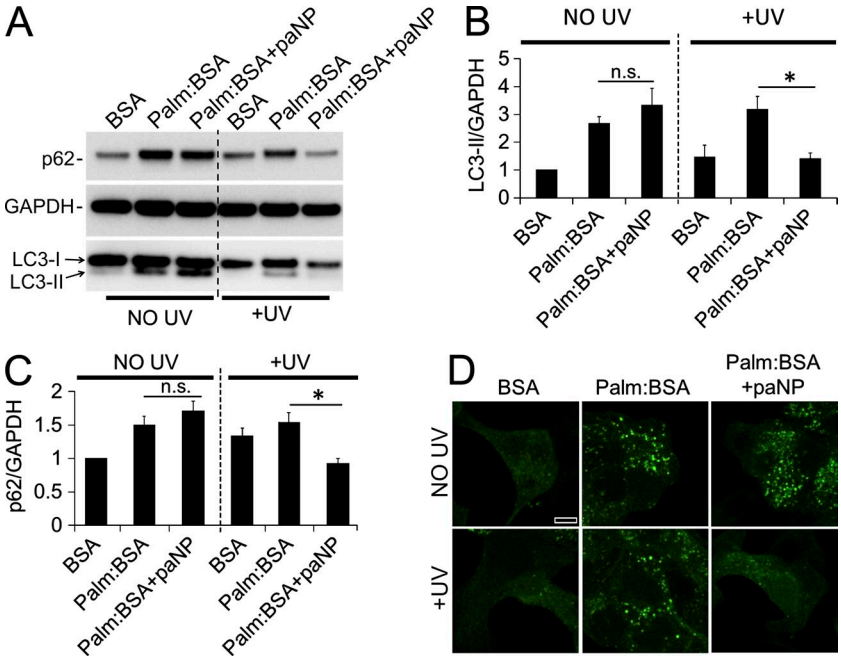

Figure 4. **Effect of paNP-induced lysosomal acidification on autophagic flux in INS1 cells exposed to palmitate.** (A–C) Western blot analysis of LC3-II and p62 protein levels in INS1 cells. Clearance of accumulated autophagosomes (LC3-II) and p62 protein is observed upon treatment with paNPs and 5 min of UV irradiation in INS1 cells exposed to palmitate (Palm:BSA) compared with control (BSA-treated) cells. Shown is the mean ± standard error; *, $P < 0.05$ between indicated conditions; n.s., not significant; $n = 5$ experiments. (D) Confocal microscopy images of GFP-LC3 expressing INS1 cells. Treatment with paNPs and 5 min of UV irradiation decreased LC3-GFP puncta accumulation under palmitate. Bar, 10 µm.

30 min before UV activation (Fig. S3 D), further supporting that the enhancement of GSIS by paNPs is mediated through enhanced lysosomal acidification.

We performed similar experiments on reaggregated islets formed from primary mouse islets (see Materials and methods). An effective concentration of paNPs in mouse islets to equate to ∼1 µg/10^4 cells used in INS1 studies corresponded to ∼5 µg/ml (calculations detailed in Materials and methods). Treatment with paNPs at 5 µg/ml for 24 h was well tolerated in mouse islets, whereas higher doses inhibited GSIS (Fig. S3 D); thus, the 5 µg/ml dose was used for GSIS studies. Notably, treatment with 5 µg/ml paNPs for 24 h followed by 5 min of UV irradiation acutely enhanced GSIS in mouse islets exposed to oleate-palmitate (Fig. 5 B).

It was previously reported that rapamycin treatment, which will up-regulate autophagosome formation (Klionsky et al., 2012; Yin et al., 2015), can improve GSIS of β-cells exposed to LT (Las et al., 2011); although previous studies have demonstrated that, under non-LT conditions, inhibiting autophagy augments GSIS (Pearson et al., 2014; Riahi et al., 2016) and up-regulating autophagy with rapamycin inhibits GSIS (Tanemura et al., 2012). Augmenting total autophagic capacity by increasing autophagosome number represents a different strategy for modulating autophagic flux under LT as compared with specifically targeting the deficit in lysosomal acidity. The paNPs show for the first time how, mechanistically, these strategies differ, yet both can have effects on autophagic flux and β-cell function during LT. It is possible that UV-activated paNPs may have effects through targets other than the lysosome, and they may exert effects independent of autophagy on β-cells. Although more work is needed to fully understand any off-target effects of paNPs, our findings in INS1 cells and primary islets demonstrate the efficacy of enhancing lysosomal acidity with paNPs on promoting autophagic flux and partially reversing β-cell dysfunction under LT. Accordingly, targeting lysosomal acidity with paNPs represents a novel strategy to improve lysosome function and autophagic flux in pancreatic β-cells exposed to LT and holds potential for treating lysosome dysfunction in other diseases where impaired autophagic flux contributes to the pathology.

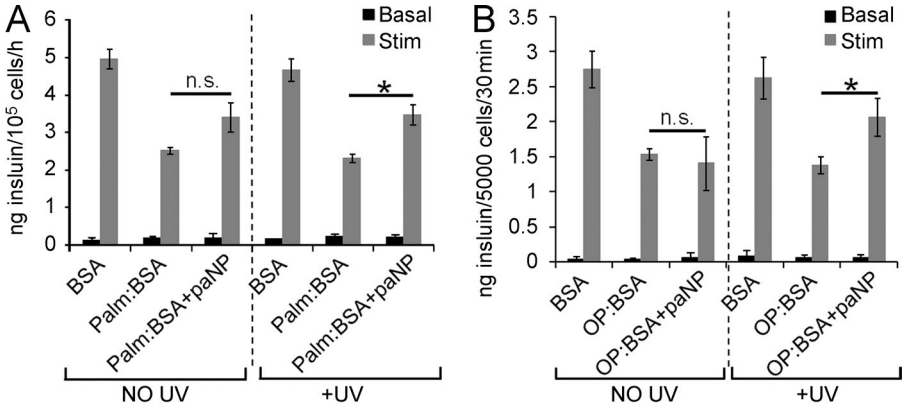

Figure 5. **Effect of paNPs on insulin secretion in INS1 cells and mouse islets exposed to fatty acid.** (A) GSIS measurements in INS1 cells exposed to palmitate (Palm:BSA) for 20 h. Treatment with 25 µg/ml paNPs (∼1 µg/10^4 cells) with UV irradiation results in significant recovery of GSIS (stimulated [Stim]: 12 mM glucose; basal: 2 mM glucose) after exposure to palmitate (Palm:BSA). Shown is the mean ± standard error ($n = 5$ experiments). (B) GSIS measurements in reaggregated mouse islets exposed to oleate-palmitate (OP:BSA) for 48 h. Treatment with 5 µg/ml paNPs (∼1 µg/10^4 cells) with UV irradiation results in significant restoration of GSIS (Stim: 16.7 mM glucose; basal: 2.8 mM glucose) after exposure to oleate-palmitate (OP:BSA). Shown is the mean ± standard error; *, $P < 0.05$ between indicated conditions; n.s., not significant; $n = 5$ experiments.

Materials and methods

Nanoparticle synthesis and characterization

All synthetic procedures were performed with minimal exposure to light. Prophylactic measures included covering the reacting vessel with aluminum foil and in general reducing the amount of light exposed to the reagents and products. All photouncaging procedures used 365-nm UV light from a Spectroline ENF-240C handheld lamp with 115 V, 60 Hz, and 200 mA (Spectronics Corp.). In brief, the light-sensitive caging moiety was prepared through methylation of 2-nitrobenzaldehyde. The subsequent secondary alcohol was added to succinic anhydride to afford the photocaged succinic acid. This succinate product was then subjected to carbonyl conjugation with the monoprotected tris(hydroxymethyl)ethane. Upon deprotection of the silyl-protecting group, the monoalcohol product was added to methacryloyl chloride to afford the final light-sensitive monomer. The 1-(2-nitrophenyl)ethan-1-ol group was selected to protect the carboxylic acid functionalities because of its fast deprotection kinetics upon photolysis and ease of synthesis. paNPs were synthesized following a previously published procedure with an oil-in-water, miniemulsion, base-catalyzed polymerization (Colby et al., 2013).

Synthesis of 1-(2-nitrophenyl)ethanol (1). To a dried round-bottom flask under nitrogen atmosphere was added 10 ml dry dichloromethane and 2-nitrobenzaldehyde (1.51 g, 10 mmol, 1.0 Eq). The solution was stirred and cooled to 4°C, upon which 10 ml of 2 M trimethylaluminum in hexanes (2 Eq) was added to the stirring solution over 10 min. The solution was allowed to warm to room temperature and stir for an additional 3 h. Subsequently, 10 ml of 0.01 M NaOH was added drop-wise to the red-orange stirring solution over an ice bath. The solution was allowed to effervesce, warm to room temperature, and stir for an additional 1 h. The solution was extracted using 0.01 M HCl and dichloromethane to yield a yellow-orange viscous liquid without further purification (96% yield). Nuclear magnetic resonance (NMR) chemical shifts for compound 1: 1H NMR [(500 MHz, $CDCl_3$): 1.33 (s, 3H), 4.06 (s, 1H), 5.17–5.24 (m, 1H), 7.25 (m, 1H), 7.47 (m, 1H), 7.68 (m, 2H)].

Synthesis of 4-(1-(2-nitrophenyl)ethoxy)-4-oxobutanoic acid (2). Succinic anhydride (201 mg, 2.0 mmol, 2.0 Eq) and 4-dimethylaminopyridine (DMAP; catalytic amount) was added to a solution of dry pyridine under a nitrogen atmosphere at room temperature. A solution of 1 was made using dry pyridine (152 mg, 1.0 mmol, 1.0 Eq, in 2 ml of solvent). The anhydride was allowed to fully dissolve, upon which the solution of 1 was added via syringe. The solution was allowed to stir for 36 h, at which time 1 M PBS at pH 7.4 was added to the solution (5 ml). The solution was allowed to stir for another 4 h, at which point it was subject to high vacuum to evaporate the pyridine. The resulting viscous liquid was subject, twice, to rotovap evaporation with toluene to azeotrope the residual pyridine. Finally, an extraction was performed using 0.01 M HCl solution and dichloromethane. The final solution was purified on a silica column to yield a tan solid (81% yield). NMR chemical shifts for compound 2: 1H NMR [(500 MHz, $CDCl_3$): 1.63 (s, 3H), 2.58–2.68 (m, 4H), 6.32–6.36 (m, 1H), 7.42 (m, 1H), 7.62 (m, 2H), 7.92 (m, 1H)].

Synthesis of *O,O′*-(2-(hydroxymethyl)-2-methylpropane-1,3-diyl) bis(1-(2-nitrophenyl)ethyl) disuccinate (3). A solution of 2-((tert-butyldimethylsilyloxy)methyl)-2-methylpropane-1,3-diol (previously prepared, 1.0 mmol, 236 mg, 1.0 Eq) and 2 (2.2 mmol, 588 mg, 2.2 Eq) in dichloromethane (20 ml) was prepared under an atmosphere of nitrogen and allowed to cool to 4°C. A catalytic amount of DMAP was added to the stirring solution. Finally, 1-ethyl-3-(3-dimethylaminopropyl) carbodiimide (EDCI; 372 mg, 2.4 mmol, 2.4 Eq) was added to the stirring solution, which was then allowed to stir overnight. The solution was extracted once with 0.01 M HCl solution and dichloromethane. The organic layer was collected and evaporated to yield a viscous yellow liquid. Without further purification, the yellow liquid was resuspended in wet tetrahydrofuran (THF; 20 ml) and placed over an ice bath with stirring. To this solution was added 1 M tetrabutylammonium fluoride in THF (2 ml, 2 Eq), which was then allowed to stir for an additional 6 h. The solution was evaporated and extracted with 0.01 M NaOH solution and dichloromethane thrice. The organic layers were collected, evaporated, and the sticky, brown liquid was subject to column chromatography to yield the desired product (yellow viscous liquid, 58% yield). NMR chemical shifts for compound 3: 1H NMR [(500 MHz, $CDCl_3$): 0.87 (s, 3H), 1.56–1.57 (d, 3H), 1.64–1.65 (d, 5H), 2.59–2.66 (m, 8H), 3.29–3.31 (q, 2H), 6.31–6.35 (q, 2H), 7.43 (m, 2H), 7.63 (m, 4H), 7.92 (m, 2H)].

Synthesis of *O,O′*-(2-((methacryloyloxy)methyl)-2-methylpropane-1,3-diyl) bis(1-(2-nitrophenyl)ethyl) disuccinate (4). A solution of methacryloyl chloride (1.1 mmol, 110 µl, 1.1 Eq) was made in 10 ml of dry dichloromethane under a nitrogen atmosphere and allowed to cool to 4°C. A solution of compound 3 (1.0 mmol, 687 mg, 1 Eq) and triethylamine (1.5 mmol, 220 µl, 1.5 Eq) was suspended in dry dichloromethane in a separate vial. The solution of 3 was added drop-wise over 30 min and allowed to stir overnight. The solution was then extracted with 0.01 M HCl solution and dichloromethane twice; the organic layers were collected and evaporated to yield a viscous, orange-brown liquid. This liquid was then subject to column chromatography to afford the desired product (yellow viscous liquid, 81%). NMR chemical shifts for compound 4: 1H NMR [(500 MHz, $CDCl_3$): 0.97 (s, 3H), 1.63 (d, 6H), 2.17 (s, 3H), 2.61 (m, 8H), 3.99 (s, 4H), 5.59 (d, 1H), 5.57 (s, 1H), 6.08 (s, 1H), 6.33 (q, 2H), 7.42 (m, 2H), 7.67 (m, 4H), 7.85 (m, 2H)]. High resolution mass spectrometry was performed using a Waters QT (hybrid quadrupolar/time-of-flight) API US system by ESI (empirical formula: $C_{33}H_{38}N_2O_{14}$; exact mass: 686.23 theoretical: 709.2221 [M^+Na]; experimental: 709.2220 [M^+Na]; error: 0.1410 ppm).

Synthesis of 4-(benzyloxy)-4-oxobutanoic acid (5). To a solution of dry pyridine under a nitrogen atmosphere was added succinic anhydride (10 mmol, 1.14 g, 1 Eq). To this stirring solution was added benzyl alcohol (11 mmol, 1.03 ml, 1.1 Eq). The solution was allowed to stir for 48 h, at which point 1 M PBS was added to the solution (10 ml). The solution was allowed to stir for another 4 h, at which point it was subject to high vacuum to evaporate the pyridine. The resulting viscous liquid was subject, twice, to a rotovap evaporation with toluene to azeotrope the residual pyridine. Finally, an extraction was performed using 0.01 M HCl solution and dichloromethane. The final solution was purified on a silica column (1:1 ethyl acetate-hexanes) to yield a white crystalline solid (88% yield). NMR chemical shifts for compound 5: 1H NMR ([500 MHz, $CDCl_3$]: 2.59 [m, 2H], 2.68 [m, 2H], 5.26 [s, 2H], 7.33 [s, 5H]).

Synthesis of dibenzyl *O,O′*-(2-(hydroxymethyl)-2-methylpropane-1,3-diyl) disuccinate (6). A solution of 2-((tert-butyldimethylsilyloxy)methyl)-2-methylpropane-1,3-diol (previously prepared, 1.0 mmol, 236 mg, 1.0 Eq) and 5 (2.2 mmol, 458 mg, 2.2 Eq) in 20 ml dichloromethane was prepared under an atmosphere of nitrogen and allowed to cool to 4°C. A catalytic amount of DMAP was added to the stirring solution. Finally, 372 mg EDCI (2.4 mmol, 2.4 Eq) was added to the stirring solution, which was then allowed to stir overnight. The solution was extracted once with 0.01 M HCl solution and dichloromethane. The organic layer was collected and evaporated to yield a viscous clear liquid. Without further purification, the liquid was resuspended in 20 ml wet tetrahydrofuran and placed over an ice bath with stirring. To this solution was added 1 M tetrabutylammonium fluoride in 2 ml tetrahydrofuran (2 Eq), which was then allowed to stir for an additional 6 h. The solution was evaporated and extracted with 0.01 M

NaOH solution and dichloromethane thrice. The organic layers were collected, evaporated, and the sticky, tan liquid was subject to column chromatography to yield the desired product (white solid, 64% yield). NMR chemical shifts for compound 6: 1H NMR ([500 MHz, $CDCl_3$]: 0.88 (s, 3H), 2.62 [s, 8H], 3.29 [s, 2H], 3.98 [s, 4H], 5.30 [s, 4H], 7.33 [s, 10H]).

Synthesis of dibenzyl *O,O′*-(2-((methacryloyloxy)methyl)-2-methylpropane-1,3-diyl) disuccinate (7). A solution of methacryloyl chloride (1.1 mmol, 110 µl, 1.1 Eq) was made in 10 ml dry dichloromethane under a nitrogen atmosphere and allowed to cool to 4°C. A solution of 6 (1.0 mmol, 500 mg, 1 Eq) and triethylamine (1.5 mmol, 220 µl, 1.5 Eq) was suspended in dry dichloromethane in a separate vial. The solution of 6 was added drop-wise over 30 min and allowed to stir overnight. The solution was then extracted with 0.01 M HCl solution and dichloromethane twice; the organic layers were collected and evaporated to yield a viscous, orange-brown liquid. This liquid was then subject to column chromatography to afford the desired product (clear viscous liquid, 76%). NMR chemical shifts for compound 7: 1H NMR ([500 MHz, $CDCl_3$]: 0.97 [s, 3H], 2.17 [s, 3H], 2.60 [s, 8H], 3.99 [s, 4H], 4.04 (s, 2H), 5.37 (s, 4H), 5.57 (s, 1H), 6.08 (s, 1H), 7.42 (s, 10H)].

Synthesis of 1,4-*O*-methacryloylhydroquinone (8). Hydroquinone (1.0 g, 9.09 mmol, 1.0 Eq) and triethylamine (4.68 ml, 3.4 g, 3.33 mmol, 3.7 Eq) were dissolved in 75 ml of CH_2Cl_2 and chilled to 0°C. Methacryloyl chloride (3.28 ml, 3.52 g, 3.33 mmol, 3.7 Eq) was then added drop-wise to the solution while stirring. The reaction mixture was allowed to warm to room temperature while stirring overnight. The mixture was washed thrice with 1 M NaOH and once with brine, then dried over anhydrous sodium sulfate. The solvent was subsequently removed using rotovap evaporation, and the product was purified by silica gel chromatography using 10:1 hexanes:ethyl acetate to give 2.24 g (white fluffy solid, 100%). Compound 8: 1H NMR ([500 MHz, $CDCl_3$]: 2.05 [s, 6H], 5.78–5.81 [s, 2H], 6.38 [s, 2H], 7.18 [s, 4H]).

UV-decaging kinetics of *O,O′*-(2-((methacryloyloxy)methyl)-2-methylpropane-1,3-diyl) bis(1-(2-nitrophenyl)ethyl) disuccinate (4). To assess the decaging kinetics of the UV-responsive monomer and control monomer, 50 µM solutions of compound 4 and compound 7, dissolved in 1:1 MeCN:H_2O, were subjected to continuous long-wave 365-nm UV irradiation. As a positive control for UV decaging of the nitrophenyl group, 4-(1-(2-nitrophenyl)ethoxy)-4-oxobutanoic acid was also investigated. Aliquots were removed and analyzed using LC-MS.

UV-responsive nanoparticle synthesis by miniemulsion polymerization. UV deprotection of the *o*-nitrobenzyl group was monitored via LC-MS with results confirming rapid photolysis under 365-nm light ($t_{1/2}$ ~2.5 min; Fig. S2). Having demonstrated that the monomer was capable of undergoing the photolysis reaction to afford carboxylic acids, we synthesized the paNPs following our previously published procedure with an oil-in-water, miniemulsion, base-catalyzed polymerization (Colby et al., 2013). Resulting particles were small with relatively monodisperse populations (100–200 nm, PDI < 0.1).

Synthesis of UV-responsive nanoparticles followed procedures previously reported by Colby et al. (2013). In brief, 50 mg of compound 4 and 0.5 mg of cross-linker 8 (1% wt/wt) were dissolved in 460 µl dichloromethane. A separate aqueous solution of 5 mg (10% wt/wt) of SDS was dissolved in 2.0 ml of pH 7.4 phosphate buffer (5 mM). The organic and aqueous phase were then combined and sonicated for 10 min at 80 W with a 1 s pulse, 2 s delay under argon atmosphere to create an oil-in-water emulsion suspension. After sonication, 20 µl of 0.2 M ammonium persulfate and 2 µl tetramethylethylenediamine were added with vigorous stirring under argon atmosphere. The system was opened to the air after 2 h, left stirring overnight, and dialyzed for 24 h in 5 mM of pH 7.4 phosphate buffer to remove excess surfactants and salts. When synthesizing rhodamine-labeled nanoparticles, 0.05 mg PolyFluor 570 (methacryloxyethyl tricarbonyl Rhodamine B; Polysciences, Inc.) was dissolved in the dichloromethane along with the monomer and cross-linker before addition of the organic phase to the aqueous phase.

Dynamic light scattering

UV-responsive nanoparticles and controls were diluted 300 times and exposed to UV irradiation. At each time point, aliquots were removed and sized using a Brookehaven dynamic light scattering instrument. All measurements were performed in triplicate (n = 3).

Scanning electron microscopy

UV-responsive nanoparticles were diluted 1,000 times and exposed this suspension to 0, 2.5, or 10 min of long-wave UV irradiation. At each time point, aliquots were plated on silicon wafers and allowed to air dry in the dark overnight. The wafers were then affixed to aluminum stubs with copper tape and sputter coated with 5 nm Au/Pd. These samples were then imaged using a Supra 55VP field emission scanning electron microscope (ZEISS) with an accelerating voltage of 2 kV and working distance of 5 cm.

Zeta potential

UV-responsive nanoparticles and controls were diluted 300 times in deionized water (final concentration of polymer 750 µg/ml) at room temperature and exposed to UV irradiation. At each time point, aliquots were removed and zeta potential measured using a Brookehaven zeta sizer instrument. All measurements were performed in triplicate (n = 3).

pH titration

paNPs were diluted in 1 mM, 10 mM, or 100 mM pH 7.4 phosphate buffer or deionized water (250 µl particles in 2 ml aqueous). Particles were stirred under exposure to long-wave UV light and the pH measured at intervals using a pH meter. All measurements were performed in triplicate (n = 3).

Cell culture

INS1 832/13 cells were cultured in RPMI 1640 media supplemented with 10% FBS, 10 mM Hepes buffer, 1 mM pyruvate, 50 µM 2-β-mercaptoethanol, 50 U/ml penicillin, and 50 g/ml streptomycin. Cells were used between passages 60 and 75.

Animals

Islet isolation was performed on 12- to 13-wk-old C57Bl6 male mice. They were housed in accordance with the Boston University Institutional Guidelines for Animal Care (IACUC no. 14855) in compliance with United States Public Health Service Regulation. Animals were fed standard chow and kept at normal housing conditions (19–22°C and a 14:10-h light-dark cycle) until death by CO_2 asphyxiation and cervical dislocation.

Islet isolation and culture

Islets of Langerhans were isolated as described previously (Wikstrom et al., 2007). Shortly, the pancreata were inflated with RPMI media containing collagenase (Roche). After 10 min of digestion at 37°C, the islets were isolated using Histopaque-1077 (Sigma-Aldrich) gradient. Isolated islets were cultured in RPMI 1640 media supplemented with 10% FBS, 50 U/ml penicillin, and 50 g/ml streptomycin.

Islet dispersion and reaggregation to form pseudoislets

After overnight incubation after isolation, islets were incubated with Accutase (Thermo Fisher Scientific) for 10 min at 37°C to disperse the islets into individual cells. To form each pseudoislet, 5,000 cells were plated in one well of a 96-well V-bottom plate. The plate was then

centrifuged at 1,000 rpm for 3 min to pellet the cells and promote pseudoislet formation. The pseudoislets were incubated overnight before starting fatty acid treatment for 2 d. The use of uniform reaggregated islets increases reproducibility by eliminating islet size and other characteristics as factors affecting islet function; concurrently, functional GSIS and other islet characteristics are maintained (Zuellig et al., 2014).

Preparation of fatty acids

Palmitate complexed to BSA. Palmitate was dissolved in DMSO, and then this solution was dissolved at 45°C in RPMI 1640 media containing 6.7% fatty acid-free BSA (EMD Millipore) to make a 4 mM (10×) stock. For control BSA conditions, a 10× stock of RPMI 1640 media containing 5% BSA and 1% DMSO was used. For the treatment conditions, the 10× stocks were added to RPMI 1640 media containing 1% FBS, 50 U/ml penicillin, and 50 g/ml streptomycin and glucose at 10 mM. The pH of the treatment medias was then adjusted to 7.4 followed by sterile filtration before treating the INS1 cells for 20 h.

Oleate-palmitate complexed to BSA. The islets were exposed to a mixture of 200 µM oleate and palmitate for 48 h. The combination of oleate and palmitate (monounsaturated and saturated fatty acid, respectively) complexed to BSA at a 2:1 ratio represents a more physiological fatty acid mixture rather than palmitate alone. Palmitate and oleate were first dissolved in 150 mM NaCl solution, then this solution was dissolved at 37°C in 150 mM NaCl solution containing 16.75% fatty acid–free BSA to make a 10 mM (50×) stock. For the treatment conditions, the 10× stocks were added to RPMI 1640 media containing 1% FBS, 50 U/ml penicillin, and 50 g/ml streptomycin and glucose at 10 mM. The pH of the treatment media was then adjusted to 7.4 followed by sterile filtration before treating the mouse pseudoislets for 48 h.

Treatment of INS1 and mouse islets with paNPs and fatty acids. Prepared paNPs were kept in dark so as not to expose to excess light. In brief before treatment, paNPs were vortexed for 10 s before diluting into the treatment medias. Cells were then incubated with paNPs for the indicated times, concurrent with fatty acid or BSA treatment. Cells were washed with media or PBS two or three times before assaying.

To determine if restoration of lysosomal acidity using paNPs would affect mouse islet GSIS, the paNP dose for mouse islets was matched to INS1 cell experiments by calculating paNP dose as (micrograms per cell) instead of (micrograms per milliliter), because this is a more accurate indicator of paNP exposure per cell. The paNP dose per cell in INS1 cells was estimated at ∼1 µg/10^4 cells as calculated: paNPs were diluted to 25 µg/ml in 100 µl solution (for one well of a 96-well plate), which contained ∼25,000 cells per well. The mouse islet experiments used only 5,000 cells per well (in one well of a 96-well plate) in the same 100-µl volume of media, so the effective concentration of paNPs to equate to ∼1 µg/10^4 cells would be 5 µg/ml for the mouse pseudoislets. UV activation of paNPs in cells was performed using a compact UV lamp, with long-wave UV at 365 nm, 115 V (model UVL-21 Blak Ray Lamp; UVP). UV exposure was performed for 5 min at room temperature with plate lids removed and the lamp placed above cells on the culture plates. The non-UV control plates were left at room temperature for the same 5 min but kept in the dark. Cells and paNP stocks were kept in the dark as much as possible to prevent ambient light exposure.

Flow cytometry

FACS was used to establish INS1 cell lines expressing GFP-LC3. INS1 cells were infected with lentivirus encoding for GFP-LC3. The cells expressing GFP-LC3 were then sorted according to GFP intensity using MoFlo Cell Sorter. GFP-LC3–expressing INS1 cells were then imaged using a confocal microscope to visualize GFP-LC3 punctate dots within cells. GFP-LC3 was excited with 488-nm laser, and emission was captured from 495 to 530 nm.

Flow cytometry analyses of rhodamine-labeled paNP-treated cells was performed with 620 FACScan. Flow data analysis was performed using FACScalibur (Beckman Coulter). Cell debris was excluded by gating on the forward and side scatter plot. The cells were trypsinized, washed twice with PBS by centrifugation at 300–400 *g* for 5 min, and subjected to flow cytometry.

Cytotoxicity

The cytotoxicity of paNPs was determined in INS1 cells. In brief, cells were loaded with paNPs for 4 h and then photoactivated (or not) with UV light for 5 min, followed by an additional 20 h of incubation. After the 20-h incubation, viability was determined using propidium iodide staining and flow cytometry. Cells were trypsinized, washed with PBS, and resuspended in PBS containing 1 µg/ml propidium iodide (Invitrogen) followed by analysis of propidium iodide–positive cells by flow cytometry. Cells resuspended in PBS alone (no propidium iodide) were used as a control to gate for propidium iodide–positive cells.

Lysosensor staining and image analysis

Cells were stained with 1 µM LysoSensor yellow/blue for 5 min followed by confocal imaging using 360-nm excitation and collecting images at the yellow wavelength range (510–641 nm) and at the range of blue wavelength (404–456 nm). The ratio between yellow and blue was calculated using Metamorph software. In brief, background noise was removed by a median filter, followed by thresholding to identify individual lysosomes. Mean yellow and blue fluorescence intensities were obtained for the identified lysosomes, and yellow/blue ratio values were calculated. Quantification of pH changes was achieved by imaging Lysosensor fluorescence in 2-(*N*-morpholino)ethanesulfonic acid buffer of varying pH and establishing a standard curve of Lysosensor fluorescence ratio to pH. In the cases where ΔpH values are shown, a separate standard curve was not obtained but changes in Lysosensor ratio were converted to ΔpH by using previous standard curve equations, allowing relative pH changes to be calculated but not absolute pH values. For representative images shown, ratio images were generated by dividing yellow and blue Lysosensor images, and contrast was adjusted identically on all images to improve visualization. Pseudocoloring was applied to increase resolution of Lysosensor ratio changes.

Magic red cathepsin L activity assay

Cells were stained with 10 µg/ml Magic red cathepsin L (MR-cathepsin L; Immunochemistry Technologies) for 1 h. The cells were then washed three times with PBS and imaged using Celigo Imaging Cell Cytometer (Brooks Life Science Systems). Red (531/40 excitation; 629/53 emission) fluorescence channel was imaged for each well. Analysis parameters for images acquired by Celigo Imaging Cell Cytometer were optimized to identify individual cells based on fluorescence. Mean fluorescence intensity per cell values were determined by the mean integrated intensity per cell values to exclude error from background pixels included in identified cell regions. At least 1,000 cells were analyzed per well, with three- to four-well replicates per experiment.

Insulin secretion for INS1 cells

Before glucose-induced insulin secretion, cells were cultured for 2 h in RPMI containing 2 mM glucose without serum. After 1 h in 2 mM glucose RPMI medium, the +UV cells were exposed to UV light for 5 min. After the additional 1-h incubation, cells were then washed and preincubated for 30 min in DMEM (XF Assay medium; Seahorse Biosciences) containing 2 mM glucose and 0.05% BSA, pH 7.4. This was followed by a 60-min incubation in media containing either 2 or 12 mM glucose. Media was collected and stored at –20°C for insulin measurement. For secretion experiments where cells were pretreated

with bafilomycin to inhibit lysosomal acidification, the normal secretion protocol was followed except a parallel set of cells were treated with 10 nM bafilomycin during the 2-mM glucose RPMI incubation.

Insulin secretion for mouse reaggregated islets

Before glucose-induced insulin secretion, islets were preincubated for 30 min in DMEM (XF Assay medium; Seahorse Biosciences) containing 2 mM glucose and 0.05% BSA, pH 7.4. This was followed by a 30-min incubation in media containing either 2.8 or 16.7 mM glucose. Media was collected and stored at –20°C for insulin measurement. Insulin was measured by HTRF insulin assay (Cisbio Bioassays).

Insulin measurements

Insulin was measured by HTRF insulin assay (Cisbio Bioassays). Because passage number affects INS1 secretion, secretion outlier values were excluded if greater or less than three SDs outside the mean of previous secretion experiments from similarly passaged INS1 cells. Cells were fixed in 4% paraformaldehyde, stained with DAPI, and imaged using Celigo Imaging Cell Cytometer (Brooks Life Science Systems) to count the total number of cells per well for normalization. Alternatively, cells were lysed in cold PBS containing 0.1% Triton X-100 (Sigma-Aldrich) and 25 mM NaOH for insulin content.

Immunofluorescent staining for insulin

INS1 cells were loaded with 100 µg/ml rhodamine-labeled paNPs for 20 h followed by fixation with 4% paraformaldehyde for 15 min. Cells were either permeabilized with 0.15% Triton X-100 in PBS for 10 min or left unpermeabilized. Permeabilization with Triton X-100 improved insulin staining but decreased rhodamine fluorescence. After blocking with 3% BSA in PBS for 30 min, cells were incubated with 1:100 insulin antibody (Cell Signaling Technology) for 60 min. After washing with PBS, cells were then incubated with 1:400 anti–rabbit Alexa Fluor 488 for 60 min. Cells were then washed with PBS and mounted on slides for imaging.

Western blot

Samples were prepared as described previously (Kimura et al., 2009). In brief, protein samples were prepared by washing cells twice with PBS on ice, followed by lysing the cells with RIPA buffer (Santa Cruz Biotechnology, Inc.) containing additional 2% Triton-X-100, protease inhibitors (Santa Cruz Biotechnology, Inc.), and 1 mM PMSF. Lysates were kept on ice for 30 min followed by centrifugation for 10 min at 13,500 *g* at 4°C. Supernatants were kept as protein samples and Bicinchoninic acid assay (Thermo Fisher Scientific) was used to determine total protein concentrations. NuPAGE 4× LDS sample buffer (Invitrogen) was added to samples followed by boiling at 95°C for 10 min. The samples were then loaded in 4–12% polyacrylamide gel (Invitrogen) and transferred onto a polyvinylidene difluoride membrane (Invitrogen) using a wet (tank) transfer machine. The membranes were blocked with 5% nonfat dry milk for 2 h and then incubated with LC3 (Cell Signaling Technology) and p62 (Cell Signaling Technology) primary antibodies according to the manufacturer's instructions. Membranes were washed with phosphate-buffered saline containing 0.1% Tween-20 and then incubated with anti–rabbit IgG secondary antibody (Cell Signaling Technology) solution (1:3,000) for 1 h or anti-mouse (1:3,000) for 1 h. The membranes were again washed and exposed to a chemiluminescent SuperSignal West Femto Maximum Sensitivity Substrate (Thermo Fisher Scientific) to detect the protein signals. Protein loading in the gels was confirmed by GAPDH antibody (1:1,000; Cell Signaling Technology), and the densitometric values were used for adjustment of any differences in loading. Densitometric analysis of the Western blot signals was performed at nonsaturating exposures and analyzed using the ImageJ gel analyzer function.

Statistics

Unless stated otherwise, error bars indicate means and standard error, and an unpaired *t* test was used to validate statistical differences between two conditions. To determine significance of multiple conditions, a one-way ANOVA with post hoc Tukey's test was used.

Online supplemental material

Fig. S1 shows the schematic of paNP synthesis. Fig. S2 shows the deprotection kinetics of paNPs, uptake into INS1 cells, and comparison to PLGA NPs for degree of lysosomal acidification. Fig. S3 shows effect of paNPs on insulin content in INS1 cells and lack of colocalization of rhodamine-labeled paNPs with insulin granules. In addition, insulin secretion results are shown demonstrating that paNPs lose their effect on GSIS once lysosomal pH is neutralized with bafilomycin treatment. Finally, titration of paNPs in mouse islets based on GSIS response is shown. Online supplemental material is available at http://www.jcb.org/cgi/content/full/jcb.201511042/DC1.

Acknowledgments

The authors would like to thank those who contributed helpful discussions and support of the research, including Drs. Victoria Herrera, Barbara Corkey, Jude Deeney, Marc Liesa, Marcus Oliviera, José Antonio Enríquez, Dani Dagan, Andrew Ferree, Kiana Mahdaviani, Gilad Twig, and Mike Kirber, as well as Dovi Shlomo and Nadine Aziz. The authors would like to thank the Evans Center and Drs. Katya Ravid and David Coleman for the support of interdisciplinary collaborative studies.

K.M. Trudeau was supported by a National Science Foundation Graduate Research Fellowship under grant DGE-0741448 and a Levinsky Fellowship from the Department of Medicine at Boston University School of Medicine. O.S. Shirihai is funded by National Institutes of Health grants RO1 DK35914, R01 DK56690, and R01 DK074778. This work was supported in part by funding from the National Science Foundation (DMR-1006601 to M.W. Grindstaff), Boston University's Nanomedicine Program and Cross-Disciplinary Training in Nanotechnology for Cancer (National Institutes of Health grant R25 CA153955, A.H. Colby), and the American Chemical Society James Flack Norris/Theodore Williams Summer Research Scholarship (J.H. Feng). G. Las was supported by the Israel Science Foundation under grant 2018/13 and by the National Institute for Biotechnology in the Negev.

The authors declare no competing financial interests.

Submitted: 10 November 2015
Accepted: 15 June 2016

References

Baltazar, G.C., S. Guha, W. Lu, J. Lim, K. Boesze-Battaglia, A.M. Laties, P. Tyagi, U.B. Kompella, and C.H. Mitchell. 2012. Acidic nanoparticles are trafficked to lysosomes and restore an acidic lysosomal pH and degradative function to compromised ARPE-19 cells. *PLoS One.* 7:e49635. http://dx.doi.org/10.1371/journal.pone.0049635

Bareford, L.M., and P.W. Swaan. 2007. Endocytic mechanisms for targeted drug delivery. *Adv. Drug Deliv. Rev.* 59:748–758. http://dx.doi.org/10.1016/j.addr.2007.06.008

Choi, S.E., S.M. Lee, Y.J. Lee, L.J. Li, S.J. Lee, J.H. Lee, Y. Kim, H.S. Jun, K.W. Lee, and Y. Kang. 2009. Protective role of autophagy in palmitate-induced INS-1 beta-cell death. *Endocrinology.* 150:126–134. http://dx.doi.org/10.1210/en.2008-0483

Colby, A.H., Y.L. Colson, and M.W. Grinstaff. 2013. Microscopy and tunable resistive pulse sensing characterization of the swelling of pH-responsive,

polymeric expansile nanoparticles. *Nanoscale.* 5:3496–3504. http://dx.doi.org/10.1039/c3nr00114h

Colson, Y.L., and M.W. Grinstaff. 2012. Biologically responsive polymeric nanoparticles for drug delivery. *Adv. Mater.* 24:3878–3886. http://dx.doi.org/10.1002/adma.201200420

Ebato, C., T. Uchida, M. Arakawa, M. Komatsu, T. Ueno, K. Komiya, K. Azuma, T. Hirose, K. Tanaka, E. Kominami, et al. 2008. Autophagy is important in islet homeostasis and compensatory increase of beta cell mass in response to high-fat diet. *Cell Metab.* 8:325–332. http://dx.doi.org/10.1016/j.cmet.2008.08.009

Fukuo, Y., S. Yamashina, H. Sonoue, A. Arakawa, E. Nakadera, T. Aoyama, A. Uchiyama, K. Kon, K. Ikejima, and S. Watanabe. 2014. Abnormality of autophagic function and cathepsin expression in the liver from patients with non-alcoholic fatty liver disease. *Hepatol. Res.* 44:1026–1036. http://dx.doi.org/10.1111/hepr.12282

Ganta, S., H. Devalapally, A. Shahiwala, and M. Amiji. 2008. A review of stimuli-responsive nanocarriers for drug and gene delivery. *J. Control. Release.* 126:187–204. http://dx.doi.org/10.1016/j.jconrel.2007.12.017

González-Rodríguez, A., R. Mayoral, N. Agra, M.P. Valdecantos, versus Pardo, M.E. Miquilena-Colina, J. Vargas-Castrillón, O. Lo Iacono, M. Corazzari, G.M. Fimia, et al. 2014. Impaired autophagic flux is associated with increased endoplasmic reticulum stress during the development of NAFLD. *Cell Death Dis.* 5:e1179. http://dx.doi.org/10.1038/cddis.2014.162

Inami, Y., S. Yamashina, K. Izumi, T. Ueno, I. Tanida, K. Ikejima, and S. Watanabe. 2011. Hepatic steatosis inhibits autophagic proteolysis via impairment of autophagosomal acidification and cathepsin expression. *Biochem. Biophys. Res. Commun.* 412:618–625. http://dx.doi.org/10.1016/j.bbrc.2011.08.012

Jaishy, B., Q. Zhang, H.S. Chung, C. Riehle, J. Soto, S. Jenkins, P. Abel, L.A. Cowart, J.E. Van Eyk, and E.D. Abel. 2015. Lipid-induced NOX2 activation inhibits autophagic flux by impairing lysosomal enzyme activity. *J. Lipid Res.* 56:546–561. http://dx.doi.org/10.1194/jlr.M055152

Kawai, A., H. Uchiyama, S. Takano, N. Nakamura, and S. Ohkuma. 2007. Autophagosome-lysosome fusion depends on the pH in acidic compartments in CHO cells. *Autophagy.* 3:154–157. http://dx.doi.org/10.4161/auto.3634

Kimura, S., N. Fujita, T. Noda, and T. Yoshimori. 2009. Monitoring autophagy in mammalian cultured cells through the dynamics of LC3. *Methods Enzymol.* 452:1–12. http://dx.doi.org/10.1016/S0076-6879(08)03601-X

Klionsky, D.J., F.C. Abdalla, H. Abeliovich, R.T. Abraham, A. Acevedo-Arozena, K. Adeli, L. Agholme, M. Agnello, P. Agostinis, J.A. Aguirre-Ghiso, et al. 2012. Guidelines for the use and interpretation of assays for monitoring autophagy. *Autophagy.* 8:445–544.

Kost, J., and R. Langer. 2001. Responsive polymeric delivery systems. *Adv. Drug Deliv. Rev.* 46:125–148. http://dx.doi.org/10.1016/S0169-409X(00)00136-8

Kroemer, G. 2015. Autophagy: a druggable process that is deregulated in aging and human disease. *J. Clin. Invest.* 125:1–4. http://dx.doi.org/10.1172/JCI78652

Las, G., S.B. Serada, J.D. Wikstrom, G. Twig, and O.S. Shirihai. 2011. Fatty acids suppress autophagic turnover in β-cells. *J. Biol. Chem.* 286:42534–42544. http://dx.doi.org/10.1074/jbc.M111.242412

Lee, J.H., M.K. McBrayer, D.M. Wolfe, L.J. Haslett, A. Kumar, Y. Sato, P.P. Lie, P. Mohan, E.E. Coffey, U. Kompella, et al. 2015. Presenilin 1 maintains lysosomal Ca(2+) homeostasis via TRPML1 by regulating vATPase-mediated lysosome acidification. *Cell Reports.* 12:1430–1444. http://dx.doi.org/10.1016/j.celrep.2015.07.050

Mir, S.U., N.M. George, L. Zahoor, R. Harms, Z. Guinn, and N.E. Sarvetnick. 2015. Inhibition of autophagic turnover in β-cells by fatty acids and glucose leads to apoptotic cell death. *J. Biol. Chem.* 290:6071–6085. http://dx.doi.org/10.1074/jbc.M114.605345

Moghimi, S.M., A.C. Hunter, and T.L. Andresen. 2012. Factors controlling nanoparticle pharmacokinetics: an integrated analysis and perspective. *Annu. Rev. Pharmacol. Toxicol.* 52:481–503. http://dx.doi.org/10.1146/annurev-pharmtox-010611-134623

Molina, A.J., J.D. Wikstrom, L. Stiles, G. Las, H. Mohamed, A. Elorza, G. Walzer, G. Twig, S. Katz, B.E. Corkey, and O.S. Shirihai. 2009. Mitochondrial networking protects beta-cells from nutrient-induced apoptosis. *Diabetes.* 58:2303–2315. http://dx.doi.org/10.2337/db07-1781

Motornov, M., J. Zhou, M. Pita, I. Tokarev, versus Gopishetty, E. Katz, and S. Minko. 2009. An integrated multifunctional nanosystem from command nanoparticles and enzymes. *Small.* 5:817–820. http://dx.doi.org/10.1002/smll.200801550

Park, H.W., and J.H. Lee. 2014. Calcium channel blockers as potential therapeutics for obesity-associated autophagy defects and fatty liver pathologies. *Autophagy.* 10:2385–2386. http://dx.doi.org/10.4161/15548627.2014.984268

Park, M., A. Sabetski, Y. Kwan Chan, S. Turdi, and G. Sweeney. 2015. Palmitate induces ER stress and autophagy in H9c2 cells: implications for apoptosis and adiponectin resistance. *J. Cell. Physiol.* 230:630–639. http://dx.doi.org/10.1002/jcp.24781

Pearson, G.L., N. Mellett, K.Y. Chu, J. Cantley, A. Davenport, P. Bourbon, C.C. Cosner, P. Helquist, P.J. Meikle, and T.J. Biden. 2014. Lysosomal acid lipase and lipophagy are constitutive negative regulators of glucose-stimulated insulin secretion from pancreatic beta cells. *Diabetologia.* 57:129–139. http://dx.doi.org/10.1007/s00125-013-3083-x

Petros, R.A., and J.M. DeSimone. 2010. Strategies in the design of nanoparticles for therapeutic applications. *Nat. Rev. Drug Discov.* 9:615–627. http://dx.doi.org/10.1038/nrd2591

Poitout, V., J. Amyot, M. Semache, B. Zarrouki, D. Hagman, and G. Fontés. 2010. Glucolipotoxicity of the pancreatic beta cell. *Biochim. Biophys. Acta.* 1801:289–298. http://dx.doi.org/10.1016/j.bbalip.2009.08.006

Riahi, Y., J.D. Wikstrom, E. Bachar-Wikstrom, N. Polin, H. Zucker, M.S. Lee, W. Quan, L. Haataja, M. Liu, P. Arvan, et al. 2016. Autophagy is a major regulator of beta cell insulin homeostasis. *Diabetologia.* 59:1480–1491. http://dx.doi.org/10.1007/s00125-016-3868-9

Schneider, J.L., and A.M. Cuervo. 2014. Autophagy and human disease: emerging themes. *Curr. Opin. Genet. Dev.* 26:16–23. http://dx.doi.org/10.1016/j.gde.2014.04.003

Tanemura, M., Y. Ohmura, T. Deguchi, T. Machida, R. Tsukamoto, H. Wada, S. Kobayashi, S. Marubashi, H. Eguchi, T. Ito, et al. 2012. Rapamycin causes upregulation of autophagy and impairs islets function both in vitro and in vivo. *Am. J. Transplant.* 12:102–114. http://dx.doi.org/10.1111/j.1600-6143.2011.03771.x

Terman, A., T. Kurz, M. Navratil, E.A. Arriaga, and U.T. Brunk. 2010. Mitochondrial turnover and aging of long-lived postmitotic cells: the mitochondrial-lysosomal axis theory of aging. *Antioxid. Redox Signal.* 12:503–535. http://dx.doi.org/10.1089/ars.2009.2598

Wikstrom, J.D., S.M. Katzman, H. Mohamed, G. Twig, S.A. Graf, E. Heart, A.J. Molina, B.E. Corkey, L.M. de Vargas, N.N. Danial, et al. 2007. beta-Cell mitochondria exhibit membrane potential heterogeneity that can be altered by stimulatory or toxic fuel levels. *Diabetes.* 56:2569–2578. http://dx.doi.org/10.2337/db06-0757

Wolinsky, J.B., Y.L. Colson, and M.W. Grinstaff. 2012. Local drug delivery strategies for cancer treatment: gels, nanoparticles, polymeric films, rods, and wafers. *J. Control. Release.* 159:14–26. http://dx.doi.org/10.1016/j.jconrel.2011.11.031

Yamamoto, A., Y. Tagawa, T. Yoshimori, Y. Moriyama, R. Masaki, and Y. Tashiro. 1998. Bafilomycin A1 prevents maturation of autophagic vacuoles by inhibiting fusion between autophagosomes and lysosomes in rat hepatoma cell line, H-4-II-E cells. *Cell Struct. Funct.* 23:33–42. http://dx.doi.org/10.1247/csf.23.33

Yin, J., L. Gu, Y. Wang, N. Fan, Y. Ma, and Y. Peng. 2015. Rapamycin improves palmitate-induced ER stress/NF κB pathways associated with stimulating autophagy in adipocytes. *Mediators Inflamm.* 2015:272313. http://dx.doi.org/10.1155/2015/272313

Zhang, Y., versus Krieger, and M. Hensel. 2015. Application of fluorescent nanoparticles to study remodeling of the endo-lysosomal system by intracellular bacteria. *J. Vis. Exp.* 95:e52058.

Zubris, K.A., R. Liu, A. Colby, M.D. Schulz, Y.L. Colson, and M.W. Grinstaff. 2013. In vitro activity of Paclitaxel-loaded polymeric expansile nanoparticles in breast cancer cells. *Biomacromolecules.* 14:2074–2082. http://dx.doi.org/10.1021/bm400434h

Zuellig, R.A., G. Cavallari, P. Gerber, O. Tschopp, G.A. Spinas, W. Moritz, and R. Lehmann. 2014. Improved physiological properties of gravity-enforced reassembled rat and human pancreatic pseudo-islets. *J. Tissue Eng. Regen. Med.* http://dx.doi.org/10.1002/term.1891